

# Fault Striae Analysis and Paleostress Reconstruction of the Northern Tectonic Province (Egyptian Nubian Shield): Insights into the Brittle Deformation History of the Northern East African Orogen

Z. Hamimi<sup>a</sup>, H. El Sundoly<sup>b</sup>, D. Delvaux<sup>c</sup>, A. Waheeb<sup>b</sup>, W. Hagag<sup>a,\*</sup>, and M. H. Younis<sup>d</sup>

<sup>a</sup> Benha University, Geology Department, Faculty of Science, Benha, 13518 Egypt

<sup>b</sup> Nuclear Materials Authority, El-Maadi, Cairo, 530 Egypt

<sup>c</sup> Royal Museum for Central Africa, Earth Sciences, Tervuren, 3080 Belgium

<sup>d</sup> Aswan University, Geology Department, Faculty of Science, Aswan, 81528 Egypt

\*e-mail: wael.hagag@fsc.bu.edu.eg

Received March 30, 2023; revised May 24, 2023; accepted June 23, 2023

**Abstract**—The Egyptian Nubian Shield (ENS), the northwestern continuation of the East African Orogen (EAO), comprises a variety of three lithologically and structurally different tectonic provinces—southern compressional-, central transpressional/wrench-, and northern extensional- provinces. The extensional tectonic province (ETP) extends from Qena–Safaga shear belt up to the northern tip of the ENS. Several lines of evidence indicate extensional regime in the ETP, such as mantle delamination-induced post-orogenic magmatism and bimodal Dokhan Volcanics, together with the pervasive E–W dyke swarms and the E–W (to ENE–WSW) oriented extensional fractures. The present work is devoted to carry out the fault striae analysis and paleostress reconstruction of the northern tectonic province (ENS) in attempt to add more contribution to the brittle deformation history of the northern EAO. Field measurements collected from six areas (I–VI) have been processed using Win-Tensor Software. Analysis of fault-slip data revealed four paleostress tensor stages (groups or regimes) that prevailed in the ENS. The stress states and related tectonic regimes are characterized by the stress regime index  $R'$  and the horizontal stress axes as follows: 1st stage: transpression ( $R' = 1.91$ ), E–W compression ( $SH_{\max} = N090^{\circ}–270^{\circ} E$ ); 2nd stage: transtension ( $R' = 1.16$ ), N–S compression ( $SH_{\max} = 174^{\circ}–354^{\circ} E$ ); 3rd stage: transpression ( $R' = 1.81$ ), NE–SW compression ( $SH_{\max} = N053^{\circ}–233^{\circ} E$ ); 4th stage: extension ( $R' = 0.31$ ), E–W extension ( $Sh_{\min} = N074^{\circ}–254^{\circ} E$ ). The 1st stage can be related to the oblique convergence between E and W Gondwanalands. The 2nd stage was probably concurrent with the N- to NNW-ward migration of the Central Eastern Desert syn-collisional delamination (triggering orogen-parallel extensional collapse) to the North Eastern Desert post-collisional delamination. The 3rd stage was controlled by the generally N–S shortening which affected the northern and central ENS, post-dating the formation of volcanosedimentary Hammamat Basins. The 4th stage is akin to retreat of the Cadomian arc and the Red Sea rifting.

**Keywords:** fault striae analysis, paleostress reconstruction, deformation history, extensional tectonic province, Northern Egyptian Nubian Shield

**DOI:** 10.1134/S001685212304009X

## INTRODUCTION

The Egyptian Nubian Shield (ENS) covers about 60000 km<sup>2</sup> of the total surface area of Egypt [22]. It extends as a NNW-oriented belt along the western flank of the Red Sea Rift from lat. 22°00" (the Egyptian–Sudanese border) to ~ lat. 28°00". Regarded many researches opinion, the Precambrian basement exposures outcropping at Southern Sinai belong to the Egyptian Nubian Shield [23]. In the Eastern Desert (ED), the Egyptian Nubian Shield is traditionally subdivided into three main provinces; North Eastern Desert (NED), Central Eastern Desert (CED) and

South Eastern Desert (SED), each of which has its own lithological, geological/geomorphological and structural aspects. These provinces are separated along two main ENE-oriented shear belts; Safaga-Qena and Nugrus-Barramiya megashears (Fig. 1).

Recently, the first tectonic map for the Egyptian Nubian Shield was constructed and discriminated three structural provinces (from south to north) [25] (Fig. 1a):

- compressional;
- transpressional;
- extensional.

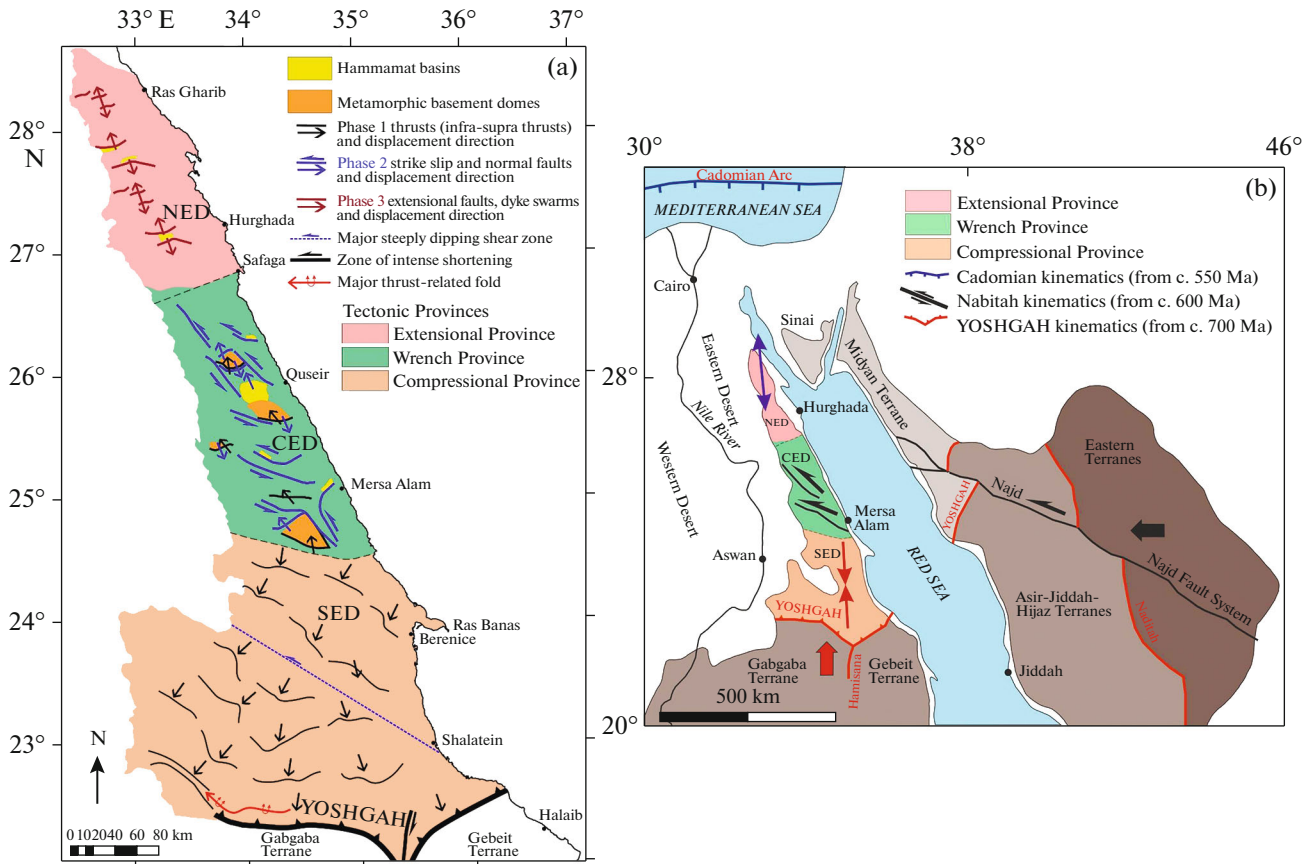


**Fig. 1.** (a) Tectonic map and structural provinces of the Egyptian Nubian Shield; (b) the three different plate tectonic far-field boundary conditions: the 1st kinematic event (between ~800 and 620 Ma) was released by the ~N–S convergence of Gabgaba–Gebait, Jiddah–Asir terranes and Eastern Desert–Midyan terranes along the the Yanbo-Onib-Sol-Hamid-G erf-Allaqi-Heiani (YOSH GAH) suture; the 2nd kinematic event (between ~640 and 580 Ma) was released by the Nabatah Orogeny when the Ad-Dawadimi–Ar-Rayan terranes of the Eastern Arabian Shield accreted to the earlier consolidated arc terranes (Afif and Tathlith terranes); the 3rd kinematic event (younger than ~580 Ma) was released by the evolution and retreat of the Cadomian Arc (after [25]).

These structural provinces have been ascribed to and interpreted within the frame of boundary conditions and flow fields into three different plate tectonic far-field boundaries (Fig. 1b):

- the 1st far-field boundary is exemplified by the Yanbo-Onib-Sol-Hamid-G erf-Allaqi-Heiani (YOSHGAH) suturing, along which the earliest magmatic-metamorphic-kinematic event (~800 and 620 Ma) was released by the ~N–S convergence of Gabgaba-Gebait, Jiddah-Asir terranes and Eastern Desert-Midyan terranes [26].

- the 2nd far-field boundary is typified by the Nabatah Suturing, along which the second kinematic event (between ~640 and 580 Ma) was released when the Ad Dawadimi–Ar Rayan terranes of the Eastern Arabian Shield accreted to the earlier consolidated arc terranes (Afif and Tathlith terranes).

- the 3rd far-field boundary is represented by the evolution and retreat of the Cadomian arc during a younger kinematic event (younger than ~580 Ma).

Structural fabric elements dominated in the southern compressional structural province include WNW–ESE to W–E oriented thrusting and imbricated thrust stacks which are well represented in vicinity of the northern flank of Wadi Allaqi.

S- (to SSW-) propagation of thrusting resulted in the formation of eye-catching thrust propagation folds, such as in Gabal Muqsim, Um Shilman and elsewhere in this province which extends up to Wadi El Gemal (south Hafafit) to the north.

In the Central transpressional structural province, the structures are gradually overprinted by Najd-related NW–SE-trending shear belts, thrusts and folds. Exhumation of the gneissic domes (metamorphic core complexes (?)) prevailing in this province (e.g. Hafafit, Meatiq, and Sibai) are transpressional shear zone-related. In the northern extensional province, a remarkable N–S extension can be evidenced by the E–W trending dyke swarms that are best observed in the voluminous granitoids (e.g. Gabal Shayeb El-Banat and Gabal Gattar), together with the predomi-

nance of the mantle delamination-related widespread post-orogenic magmatism.

Although the northern part of the Egyptian Nubian Shield (ENS) was the target for many studies, the deformation history of this Northern Tectonic Province (NTP) is still vague. Such situation comes from the fact that this gigantic province is mainly composed of voluminous intrusive bodies of post-orogenic granitoids, which were highly obliterating the outcrops and associated structures of the oldest rock units demarcated elsewhere in central- and southern- tectonic provinces of the ENS.

In addition, the main tectonic structures in the NEP are faults, extensional and shear fractures, as well as mesoscopic to minor folding of the volcano-sedimentary Hammamat Group.

As we recognize the presence of various faults and fractures, we want to elucidate the brittle tectonic evolution of the area in order to highlight what kind of tectonic stresses controlled the development of these fractures, and the geodynamic causes of these stress fields.

We intend to provide new insights into the problem of overprinting tectonic phases/stages deforming the exposed and unexposed basement units in the northern ENS. We want also to examine the validity of the widely used concept that the northern ENS is an extensional structural domain based on the mode of formation and geochemistry of the exposed rock units [11].

To this aim, we will concentrate on the analysis of the brittle structures (faults and shear fractures/zones) observed and measured in six representative areas in the NTP. These fault-slip data (fault striae, shear and tension fractures) will be analyzed for paleostress reconstruction, applying the well-known and powerful Win-Tensor Software [6, 7].

## GEOLOGICAL SETTING

### *Landsat-Based Lithologic Mapping*

Processing techniques are applicable for scene subsets of Operational Land Imager (OLI) aboard on Landsat 8 [45] and Granule ID using ENVI software, version 5.1 [44]:

- Granule ID: LC81750412021278LGN00, Path 175/Row 41, acquired on October 13, 2021;
- Granule ID: LC81740422021287LGN00, Path 174/Row 42, acquired on October 15, 2021;
- Granule ID: LC81740412021335LGN00, Path 174/Row 41, acquired on December 09, 2021).

The three OLI subsets have been merged in one mosaic. Then, OLI data has been processed using several techniques such as:

- Optimum Index Factor (OIF);
- False Color Composite (FCC);
- Principle Component Analysis (PCA);

- Minimum Noise Fraction (MNF);
- Band Ratioing (BR).

The resulted gray-scale and false colored images have been interpreted to give information about the lithology of the rock units which are presented in the study area.

**Optimum Index Factor.** Applying the OIF algorithm for the seven OLI reflected (VNIR–SWIR) bands led to six color combinations with highest OIF values. The processed color composites are best to discriminate between the varieties of the rock units and separate clearly the different lithologies in the study area (Fig. 2a).

**Principal Component Analysis.** The Principal Component Analysis (PCA) technique illustrates the maximum contrast in appearance of features from several multispectral bands with simply RGB combination of three PC images. The resulted PCs equal the number of the analyzed multispectral bands. The RGB color combination of OLI PC1, PC3, and PC2 clearly discriminates the Dokhan Volcanics with dark blue color and the younger granitoids with yellowish blue color (Fig. 2b). The RGB color composite OLI-PC image (PC1, PC3, and PC5) effectively delineates the undifferentiated Quaternary deposits with yellow color, Hammamat Sediments with violet color. The younger granitoids and older granitoids show various degree of yellowish blue color (Fig. 2c).

**Minimum noise fraction.** The Minimum Noise Fraction (MNF) transform is applicable for equalizing the noise in the imagery data and reducing computations required for successive image processing (ENVI). The processed color composite image of OLI data (MNF1, MNF2, MNF3) obviously discriminates the older granitoids rocks (greenish color) and the Dokhan Volcanics with pink color (Fig. 2d).

**Band ratioing.** Band ratioing is a mathematical transformation technique dividing the DN values of pixels in one band by the DN values of equivalent pixels in another band [37]. On the OLI FCC image (6/7, 6/2, 6/5\*4/5), older granitoids have dark green color, younger granitoids show pale green color, while metagabbro and basic metavolcanics appear with blue color (Fig. 3a).

On the other hand, ophiolitic metaultramafics and related talc carbonate rocks are obviously delineated with red and rose image signatures. The OLI FCC ratio image (6/7, 5/6, 4/2) of [2] clearly discriminates the granitoids with violet color, Hammamat Volcanosedimentary sequence with greenish yellow and Dokhan Volcanics with green color (Fig. 3b).

### *Field Relations and Ground Truth*

The geologic map of the concerned area based on processing of remotely sensed data and ground truth, is the presented in our work (Fig. 4). Most, but if not all, litho-units dominated in the ETP are represented.



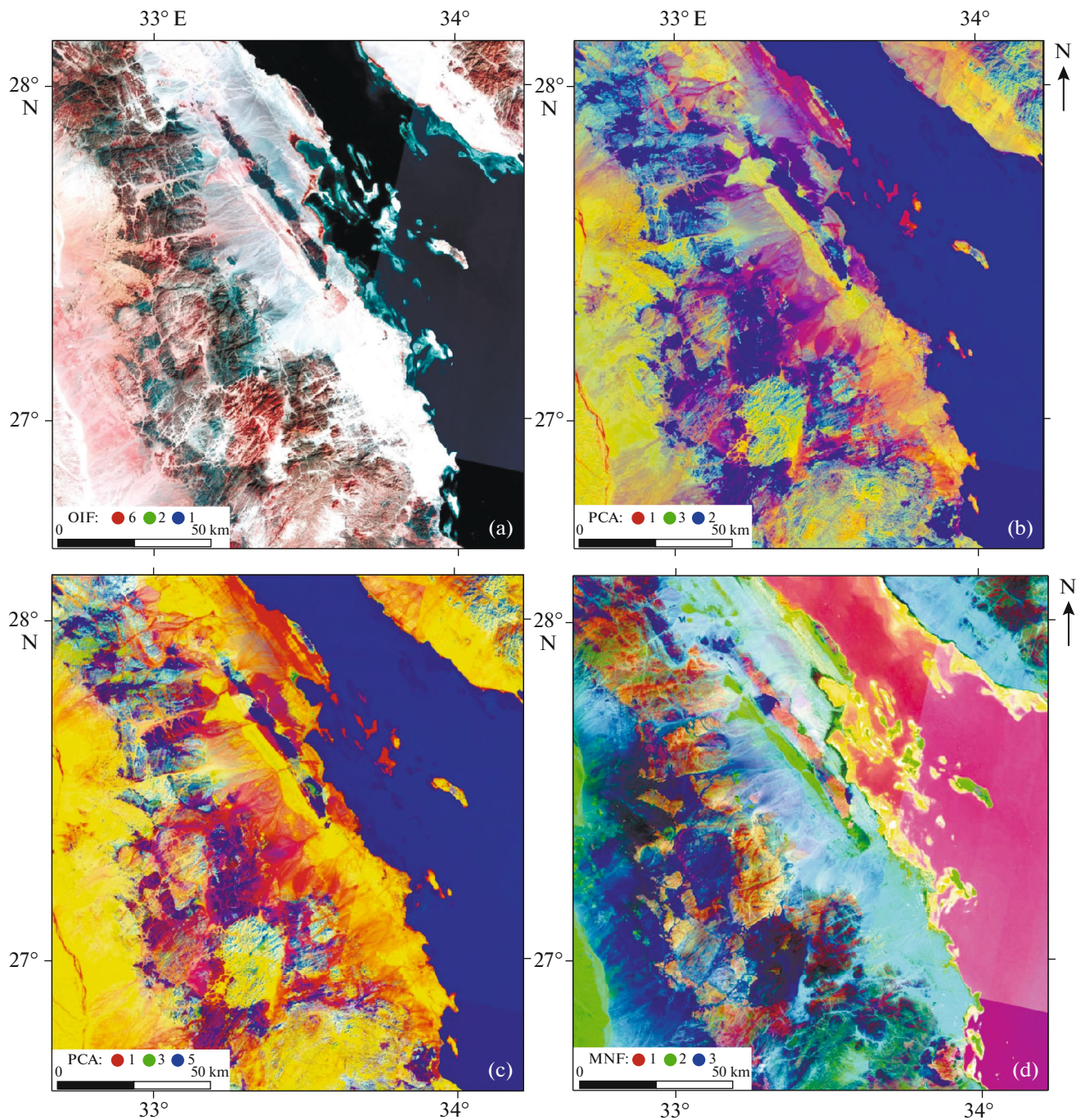


**Fig. 2.** Landsat-based lithologic discrimination of the study area. (a) Optimum Index Factor (OIF), (b) and (c) Principal Component Analysis (PCA), (d) Minimum noise fraction (MNF).

Based on cross-cutting relations and field observation the exposed units outcropping at the study area can be arranged into (from oldest to youngest):

- gneisses, migmatites and gneissose granites (Figs. 5a, 5b);
- ophiolitic group (metaultramafics and talc carbonates, mafic metavolcanics and metagabbros), island arc suite (volcaniclastic metasediments, metagabbros-

diorite complex, calc-alkaline granites), Dokhan Volcanics (Fig. 5c);

- Hammamat sediments, younger gabbros and younger granitoids (Fig. 5d).

The previously mentioned lithologies are traversed by E–W mafic to acidic dyke swarms.

The gneissose tonalite-granodiorite is remarkably foliated showing preferred quartz and feldspar mineral



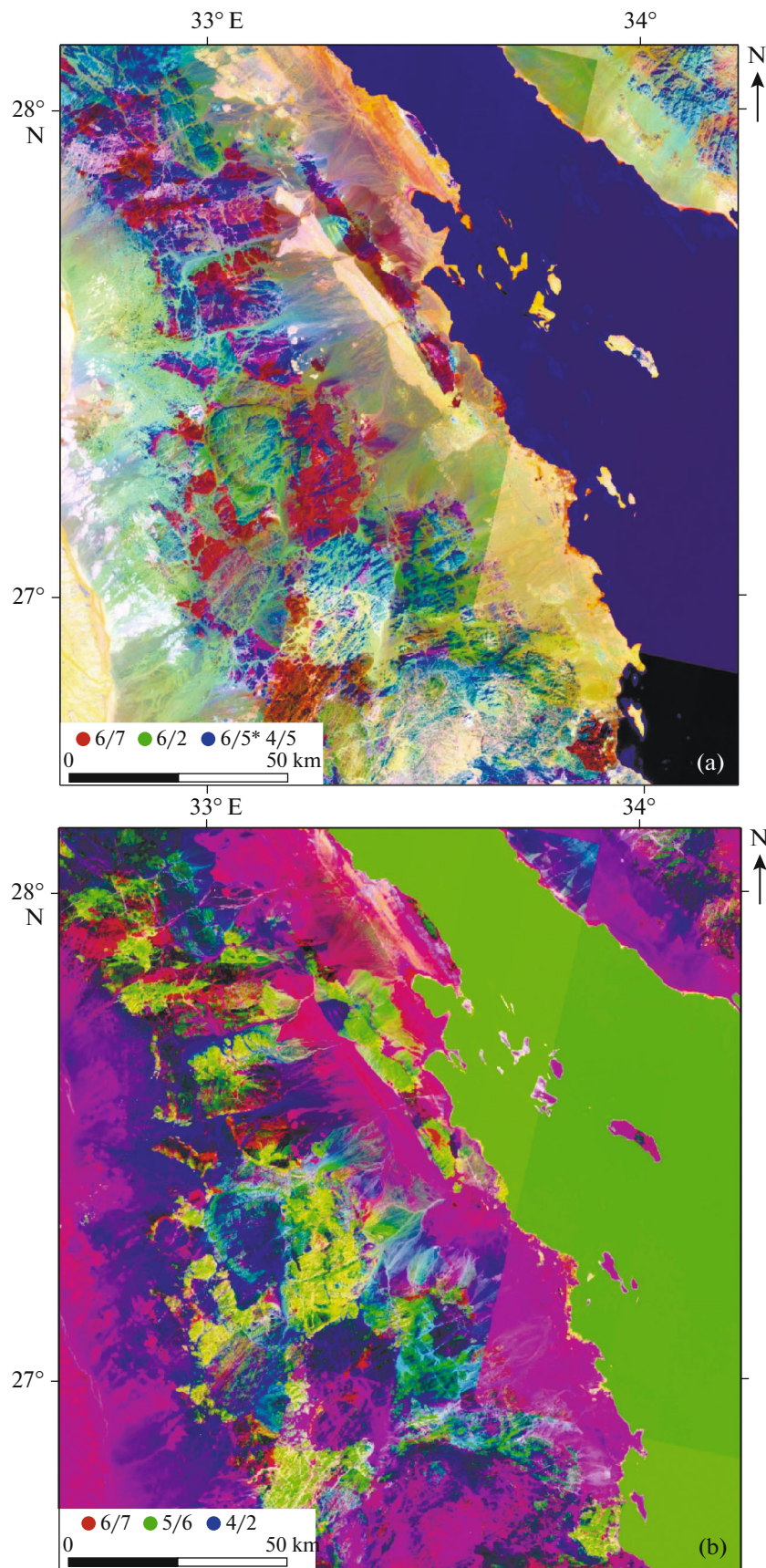


**Fig. 3.** Band Ratios: (a) Discrimination of older and younger granitoids, metagabbros and metavolcanics; (b) discrimination of granitoids, Hammamat Volcanosedimentary Sequence and Dokhan Volcanics.

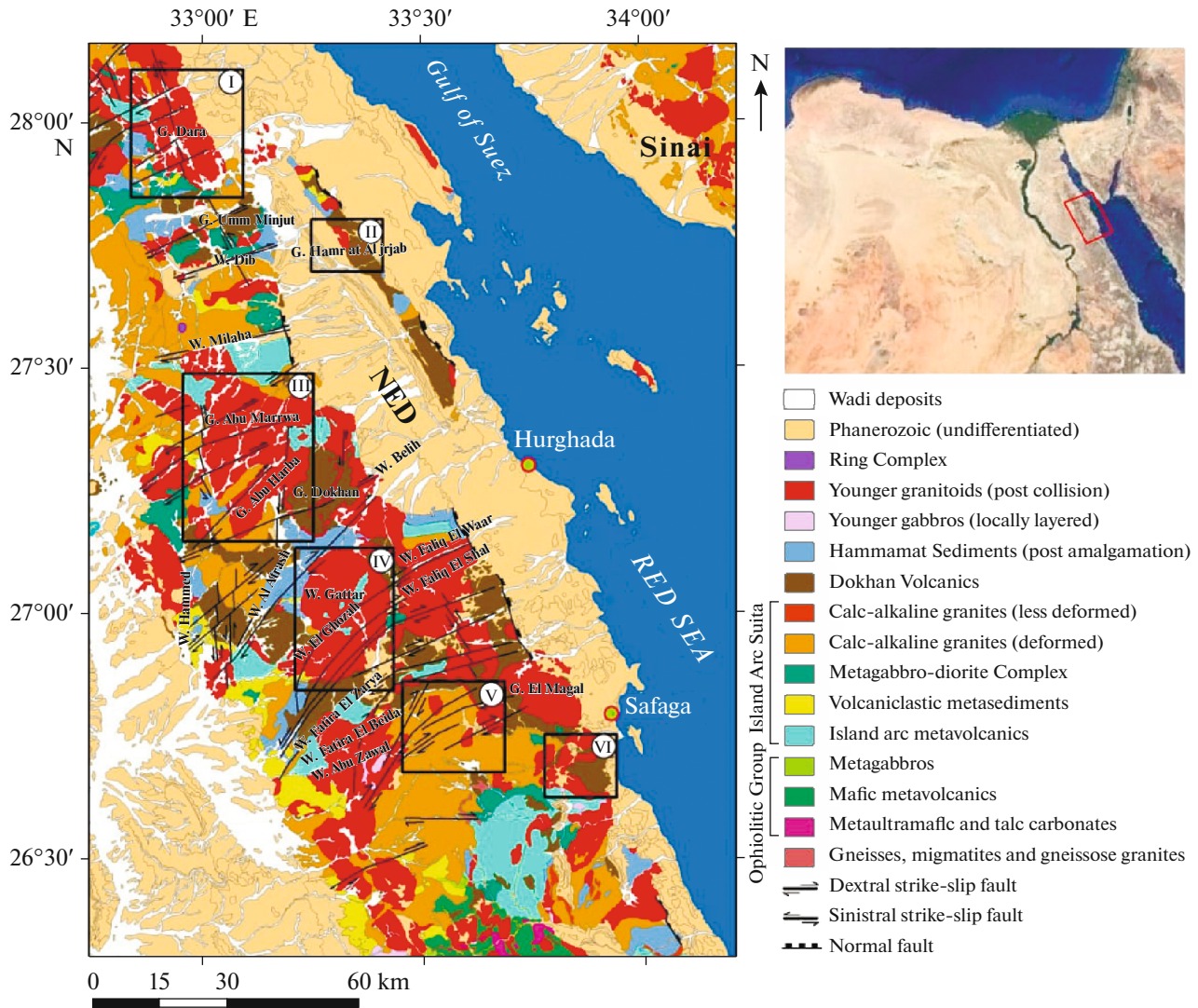


**Fig. 4.** Geologic map of the study area showing litho-units and main faults, together with the six areas from which the paleostress data have been collected.

lineation, shear bands and intrafolial folds. Geochemical studies carried out by many researches [13, 33] revealed subduction-related volcanic arc origin.

The ophiolitic group is dismembered and uncommon in the study area, being represented by metaultramafics and talc carbonates, mafic metavolcanics and metagabbros. The metaultramafics and metavolcanics are encountered in the extreme southern part of the map. They are tectonically mingled with each other. The metagabbros exist as variably-sized blocks incorporated within the volcaniclastic metasediments and the arc metavolcanics. The volcaniclastic metasediments form small outcrops distributed in the study area. They comprise greywackes and mudstones, and are slightly deformed being foliated, lineated and folded.

The older calc-alkaline (island-arc) granitoids are believed to be emplaced throughout an active subduction stage (850 Ma (?)-610 Ma, after [12, 27, 34, 41]).

They are encountered in the study area in the vicinity of Safaga-Qena asphaltic road and to the west of Esh El-Mallaha, as deformed and less deformed varieties. These varieties encompass quartz diorite, granodiorite and tonalite, together with less common monzogranite.

Contacts of the older granitoids versus the preexisting litho-units are frequently defined by chilled margins, off shoots and apophyses. The Dokhan Volcanics are encountered in the mapped area at their type locality Gabal Dokhan, besides some other mappable and unmappable outcrops. These volcanics are calc-alkaline and are regarded to be erupted at the end of the post-collisional stage in the ENS. They include flows and sheets of basaltic andesites, dacites, rhyolites, interbedded with pyroclastics (mainly tuffs, welded banded ignimbrites, volcanic breccia and agglomerates).



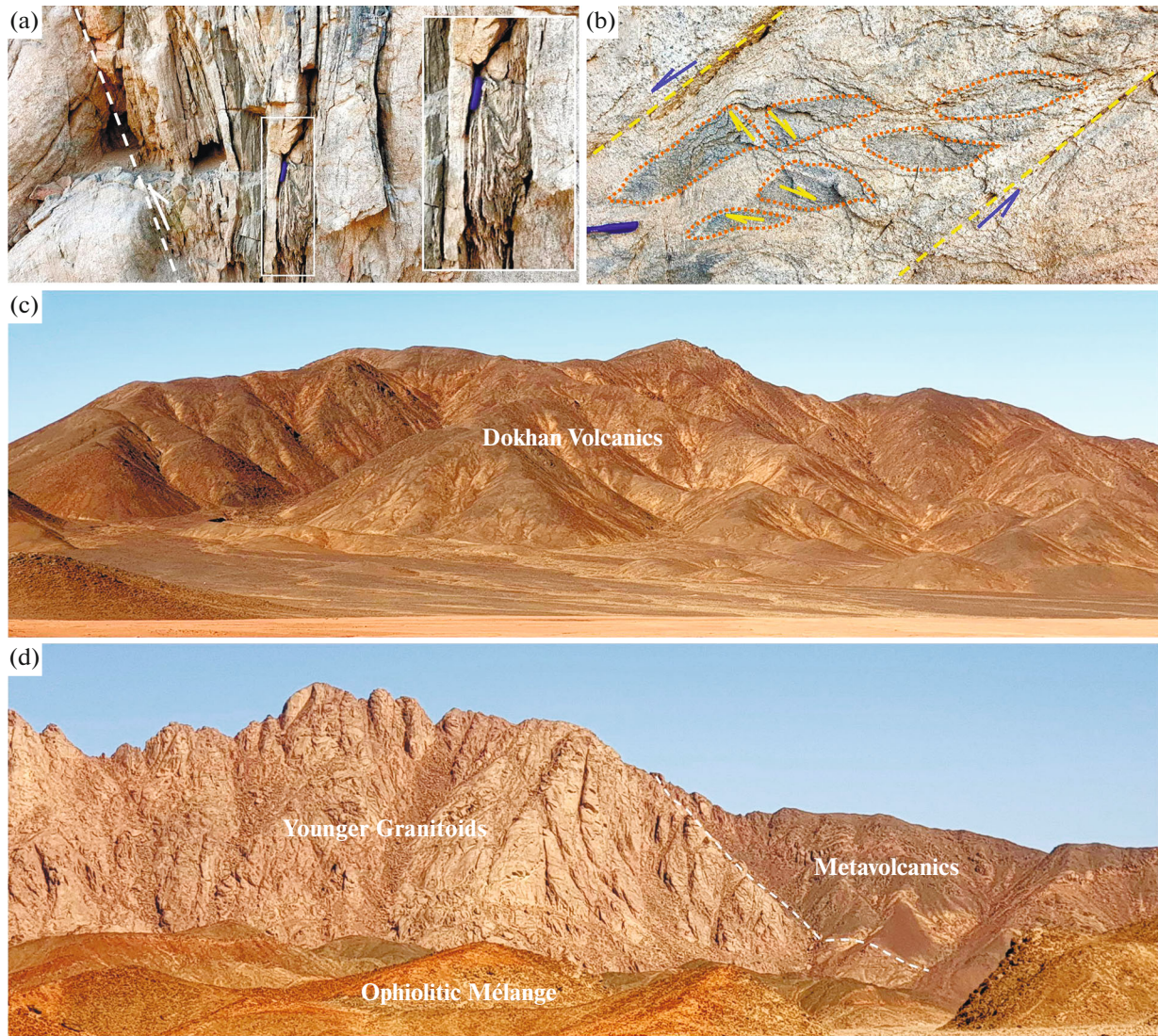


**Fig. 5.** (a) Migmatitic gneisses with thrust-related folding. (b) ductile normal shear with top-ENE displacement that formed during transensional regime; (c) an outcrop of Dokhan Volcanics in northern part of Hamrat Al Jirjab; (d) contact between younger granitoids and the metavolcanics, ophiolitic mélangé rocks exist as low mountainous blocks.

The late Ediacaran molasse-type Hammamat Sediments (632–590 Ma, after [24, 29, 42]) exist in various isolated post-amalgamation small basins and exposures, such as those recorded in Esh El-Mallaha Range, Wadi Dara, Wadi Dib, Gabal Um Tawat and Gabal El-Urf. They are mainly volcanosedimentary sequences post-dating (in places synchronous with) the eruption of the Dokhan Volcanics. The relation between the Hammamat Sediments and the Dokhan Volcanics vary from exposure to another. In places the Hammamat Sediments are unconformably overlain the Dokhan Volcanics, whereas in others both are interfingering with each other. The younger gabbros occur as small exposures in the southern part of the mapped area and in Wadi Abu Zawal and Wadi Fatira

El-Beida. They are non-deformed, showing sharp contact against other units.

Voluminous post collisional younger granitoids occur in the mapped area. These granitoids are chiefly biotite granite, syenogranite (e.g. 605 Ma Gattar- and the 595 Ma Abu Harba-syenogranite), monzogranite, alkali feldspar granite, granodiorite and quartz monzogranite. They intrude the Dokhan Volcanics and the Hammamat Sediments, as well as the oldest units. They are themselves intensively fractured, and traversed by dyke swarms of felsic to mafic composition, and sometimes by pegmatite bodies. Only one small ring complex (~2 km diameter) occurs near Wadi Dib.

This complex identified for the first time by Francis [16] and has been the subject matter of numerous stud-



ies later on in terms of its tectonic setting. Several studies [1, 18, 28] proposed an active continental margin setting during the stages of the Pan-African Orogeny. It consists of successive incomplete ring sheets (steepen from margin toward the inner) of syenite and pegmatitic syenite, encrusting an inner ring of quartz syenite, with a trachytic intermeditate ring in between. It is dissected by a number of NNW-oriented dyke swarms (felsic to mafic) nearly parallel to the Red Sea Rift.

## STRUCTURE

Structural field investigations reveal the presence of different kinds of faults that traverse most of the previously mentioned lithologic units, particularly gneisses and gneissose granites, ophiolitic group, and older and younger granitoids, with widespread slip lineations and kinematic indicators (en-echelon fractures, duplex, relay ramps), alterations and element mobilization (epidotization to quartz veining and brecciation and cataclasis). These structures are mainly strike-slip and normal faulting that sometimes exist as conjugate pairs (Figs. 6a, 6b).

Some of them show a remarkable slip, whereas others are mostly reactivated. Among evidence supporting reactivation are the overprinting of the subhorizontal slickenlines by nearly vertical ones and the presence of sheared mineral (mainly calcite and tremolite) fibers with chatter marks. Besides, flower structures are occasionally observed along some fault zones, mainly at stepover and tip zones.

They are generally negative, with concave-upward shape and rarely positive (with convex-upward shape) (Figs. 5d, 6c). Parallel to some faults are joints with plumose structures on their surfaces. Moreover, fault-related folding is infrequently recorded, especially in the southern part of the mapped area.

Based on the geometry of faulting and the observed cross-cutting and overprinting relations, we can see that we have a combination of normal faulting and strike-slip faulting. The dominant fault trends can be arranged from oldest to youngest into NNW–SSE (to NW–SE), E–W and NNE–SSW and NE–SW, and N–S to NNW–SSE (Figs. 7, 8a). The NNW–SSE (to NW–SE) faults are Najd-related Shear System, exhibiting sinistral sense of shearing (Fig. 8b).

In these faults, a combination of subhorizontal slickenlines with dip-slip to oblique-slip slickenlines with reverse movements can easily be recorded. Sometimes, they are associated thrust-related minor folding. The E–W and NNE–SSW faults dextrally displaced the NNW–SSE (to NW–SE)-oriented dykes, and quartz and pegmatite veins. These faults remarkably traverse the previously mentioned faulting trends. On the map scale, effect of these faults can easily be confirmed where the eastern edges of the Neoproterozoic belt are emerging along the planes of these faults.

## METHODOLOGY OF PALEOSTRESS RECONSTRUCTION

Fault-slip data have been investigated in six distinct areas in order to analyze the fault kinematics and reconstruct the tectonic stress that prevailed during faulting (Fig. 4).

There is a long-standing debate whether the interpretation of fault slip data in terms of strain or stress [31, 36, 38]. Following a purely kinematic approach, strain or strain rate are determined rather than stress. But the limitation of this method is that we do not have indications on the amount of displacement on each measured fault. Following the dynamic approach, reduced paleostress tensors are reconstructed from the fault-slip data under a series of assumptions [14]. It should be clear that the stress is an instantaneous physical quantity that cannot be derived from solely kinematic studies. However, from fault slip data as presented here the 4 components of the reduced stress tensor, orientation of principal axes and their relative magnitude can be derived.

We used the classic method for paleostress reconstruction based on rock mechanics [4, 10, 31, 35]. It relies on the fact that the geometry of faulting is determined by four parameters of the stress tensor that generated them: the orientation of the three principal stress axes  $\sigma_1$ ,  $\sigma_2$ ,  $\sigma_3$  and the ratio of their relative magnitude  $R$  ( $\sigma_2 - \sigma_3 / \sigma_1 - \sigma_3$ ) [5]. Inversely, knowing a set of diversely oriented faults and fractures, it is possible to reconstruct these four parameters which form the reduced paleostress tensor. We used the Win\_Tensor program [6, 7] with the methodology described in [9] and applied in many case studies [8, 30].

In Win\_Tensor [6, 7], the rotational optimization iterative method was used with the F5 function which simultaneously minimizes the angular deviation between the observed and resolved slip direction and promotes slip on fault planes. An advantage of this technique, implemented in the Win\_Tensor program [6, 7], is that incompatible datasets can be sorted out from the bulk of data and hence different populations of faults and slickensides i.e. different stress regimes can be extracted.

The stress orientation is plotted on the figures as the horizontal stress orientation,  $SH_{\max}$  for the maximal horizontal stress or  $Sh_{\min}$  for the minimum horizontal stress as computed following [32].

The global stress pattern or stress regime is based on the relative stress magnitudes which determine the type of deformation [43]. In function of the nature of the vertical stress axis ( $S_v$ ), the latter is defined as normal, strike-slip and reverse/thrust faulting [3].

Using the 4 parameters of the reduced stress tensor, we compute the parameter  $R'$  [8] which is an elegant way to display  $R$ -values for different tectonic stress regimes where  $R' = R$  for normal faulting regimes when  $\sigma_1$  is vertical,  $R' = 2 - R$  for strike-slip regimes

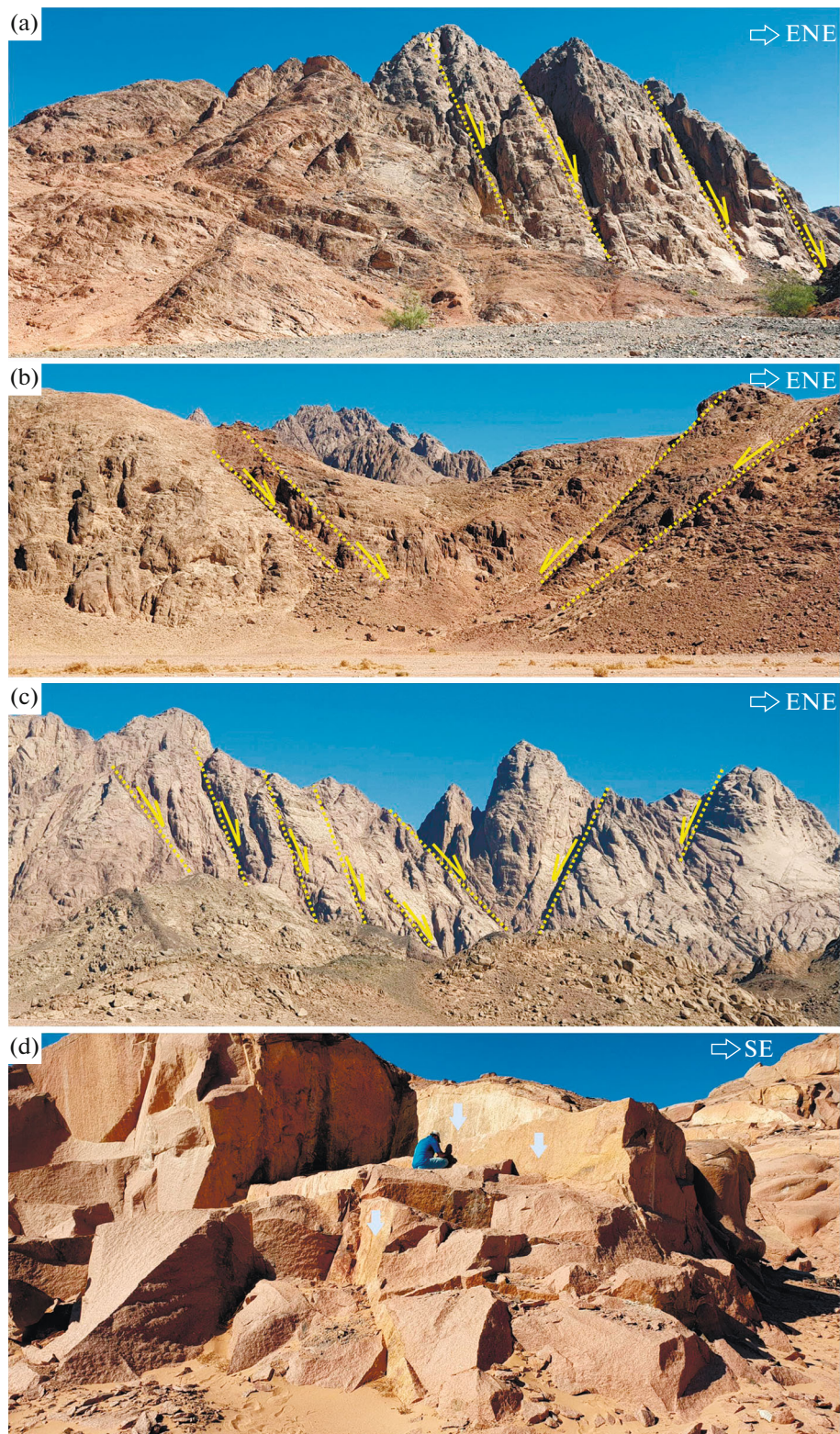


**Fig. 6.** (a) NW–SE to NNW–SSE faulting in Gabal Abu Harba (area IV); the fault planes are marked by intensively weather dykes; (b) well-developed conjugate pair of NNW–SSE faulting in the alkaline granitoids of Hamrat Al Jirjab (area II); (c) negative flower structure in the younger granitoids outcropping at the (area I); (d) NW–SE normal faulting (area II).



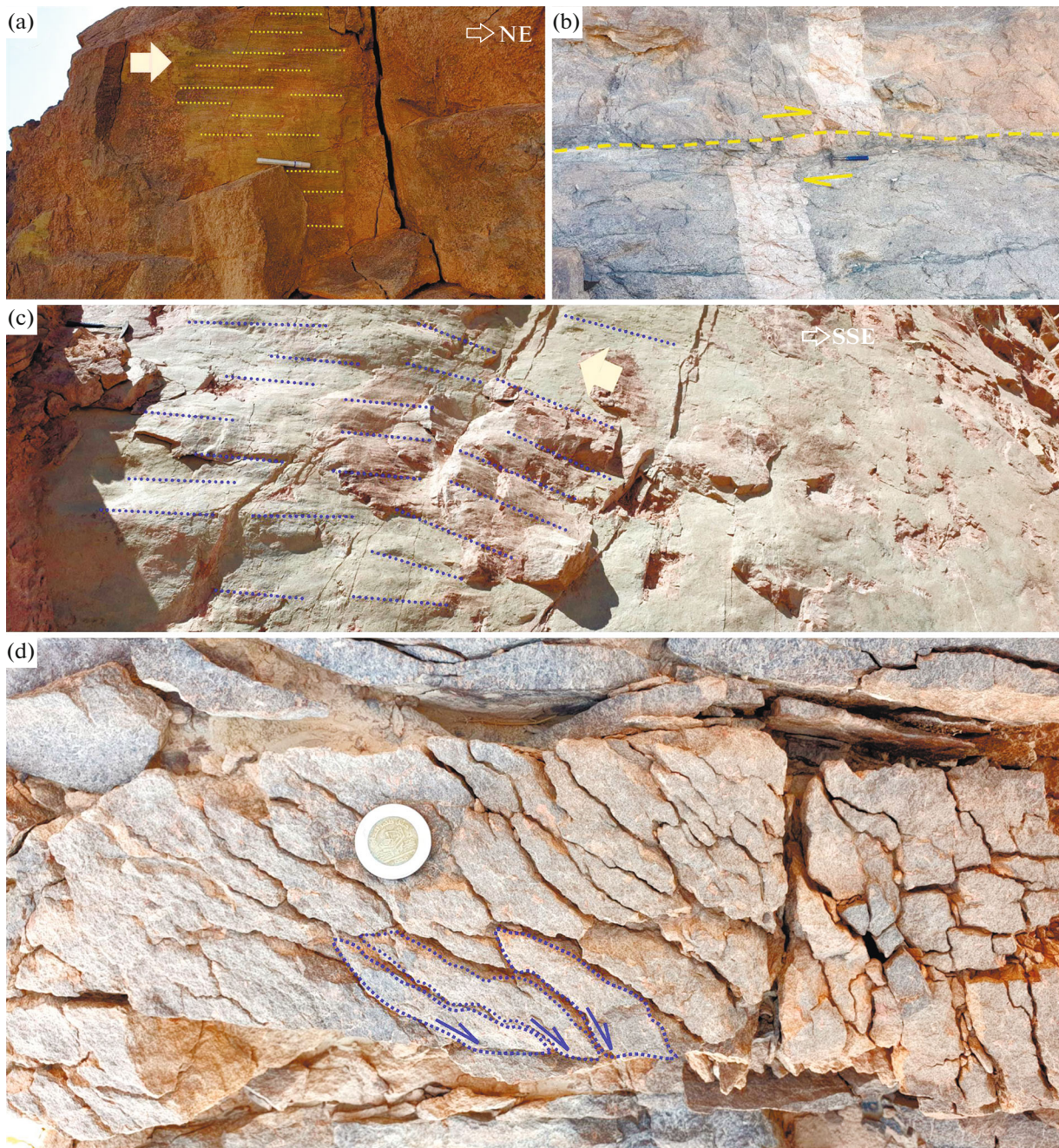


**Fig. 7.** (a) Subhorizontal slickenlines recorded along the NE–SW oriented minor fault planes reflecting dextral sense of shearing in area VI, (b) dextral offsetting of leucocratic granitic dykes (top view); (c) slickenlines exhibiting sinistral sense of shearing along the NNW–SSE fault plane: the switching of these lineations from nearly horizontal (left view) to oblique (right view); (d) sigmoidal kinematic indicators with monoclinic symmetry reflecting extensional setting.

( $\sigma_2$  is vertical) and  $R' = 2 + R$  for reverse/thrust faulting regime regimes ( $\sigma_3$  is vertical).

A shape factor  $R = 0$  ( $R' = 0$  or  $2$ ) defines a prolate shape of the stress ellipsoid,  $R = 1$  ( $R' = 1$  or  $3$ ), an oblate shape of stress ellipsoid and intermediate values, a tri-axial geometry. A strike-slip stress regime with oblate shape of the stress ellipsoid has the form  $SH_{max} \gg Sh_{min} = S_v$  and can produce a combination of strike-slip and thrust faulting, whereas a stress field of

the form  $SH_{max} \gg Sh_{min} = S_v$  and produces a combination of strike-slip and thrust faulting [43].

As we know from field observations that the fault data belong to different subset, we separate the data into subsets on the basis of which a separate stress inversion was performed for each subset. This was done in an iterative way, using the initial stress tensor as note to attract compatible data.



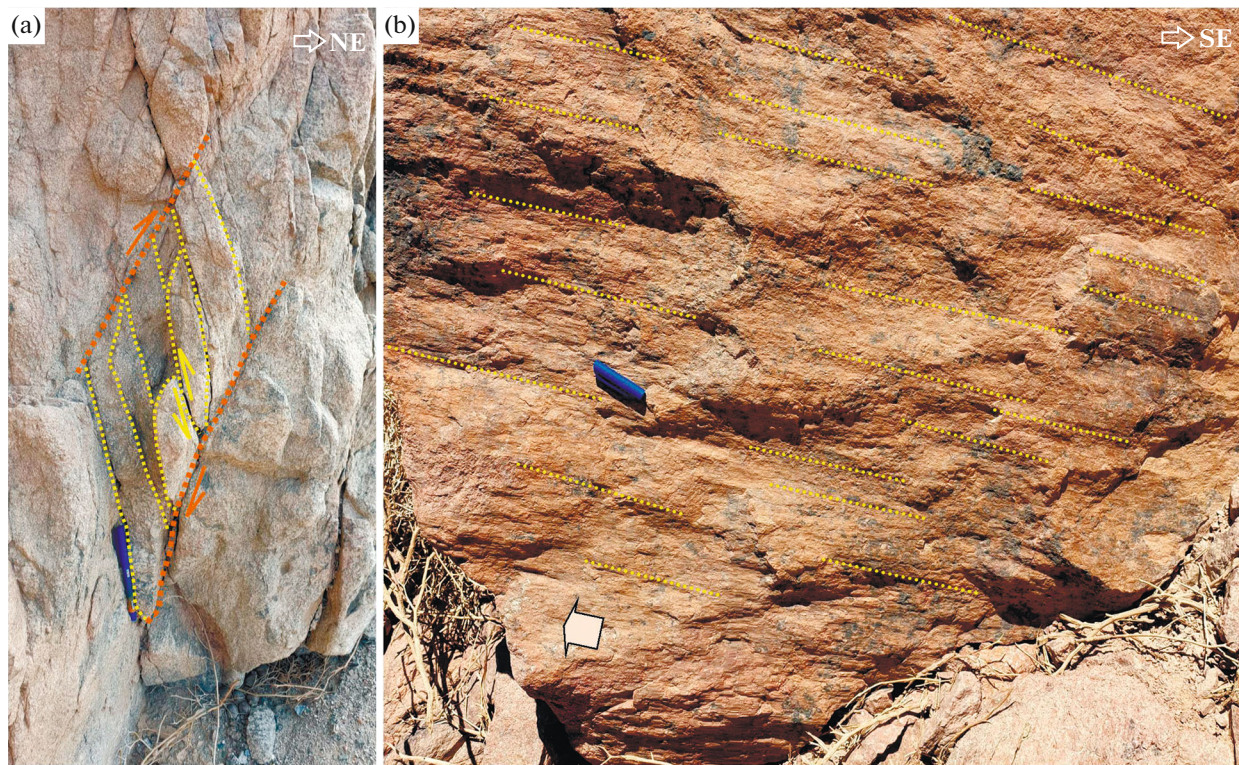


**Fig. 8.** (a) The domino structure reflecting dextral sense of shearing along a NE–SW oriented fault zone (top view); (b) Oblique striations indicating sinistral sense of shearing along the NW–SE Najd-related fault zone.

The stress tensor is differentiated not only on the basis of the orientation of the stress axes, but also on then stress ratio  $R$ . After the final determination of fault subset and their stress tensor, we made a cross-check to verify that the fault-data have been attributed to the correct subset by applying the related stress tensor to the data and calculating the resolved normal and shear stress magnitudes and orientations. As a starting point, we used the field observations (e.g., cross cutting and overprinting relationships) to build the initial subsets.

#### FAULT KINEMATIC ANALYSIS AND PALEOSTRESS RECONSTRUCTION

A total of 245 fault surfaces have been measured in 6 different field areas. Faults of each area have been processed independently. They have been separated in homogeneous and compatible subsets during the inversion process manually, in an iterative way and with cross-check to verify the fault separation. The relative chronology was established using fault and striae cross-cutting relationships. A total of four successive paleostress states have been identified.

Only in one case (Area V, 1st stage), we used the PBT method implemented in Win\_Tensor [6, 7] because the data set contain only one group of similarly oriented faults and striae (Table 1). It is a purely

kinematic approach using the P and T axes associated to each fault, for which strain rather than stress is derived [39]. In most cases, the strain axes obtained by the PBT method are similar to the ones derived by stress inversion [14]. In this case, the stress tensor inversion cannot be applied and PBT method provides a good estimation instead.

The results are presented for each area and organized in function of the identified stress stages. They are presented in stereograms for the directional part and in Mohr circles for the relative stress magnitudes on the fault-data. The stereograms represent the fault planes as great circles and their slickenlines as white dots with arrows. The resolved shear stress obtained by the application of the best-fit stress tensor on the fault population is displayed as purple striae. The red sector arc displayed on the external circle of the stereogram show the 1 sigma uncertainty in the orientation of the horizontal principal stress ( $SH_{max}$ ). The histograms represent the distribution of the values of the misfit function  $F5$ . The stress axes are shown as filled circles in a red circle for  $\sigma_1$ , red triangle for  $\sigma_2$  and red square for  $\sigma_3$ . The arrows represent the horizontal stress axes, red for the minimum stress (tension), green for the intermediate stress and blue for the maximum stress (compression). The triangular Frohlich diagram [17] shows the type of fault (black dots) and the stress regime of the best-fit tensor

**Table 1.** Paleostress states (stages) identified from the processing of fault-slip data of each area and for all areas together, using Rotational Optimization method and Win\_Tensor program [6, 7].

Area/ Stage	Method	n	nt	S1pl	S1az	S2pl	S2az	S3pl	S3az	R	R'	R'_StD	SH <sub>max</sub>	SH <sub>min</sub>	SH_StD	Regime	Stress Regime
1st Stage: E–W Transpression																	
Area I	Rot. Optim.	26	55	1	96	75	189	15	6	0.09	1.91	0.17	96	6	3.8	SS	Compressional STRIKE-SLIP
Area III	Rot. Optim.	13	55	11	82	79	266	1	172	0.55	1.45	0.29	82	172	6.2	SS	Pure STRIKE-SLIP
Area IV	Rot. Optim.	15	36	28	243	56	103	19	343	0.77	1.23	0.24	71	161	13.6	SS	Extensional STRIKE-SLIP
Area V	PBT	6	34	11	265	61	154	26	0	0.5	1.5	–	86	176	4.8	SS	Pure STRIKE-SLIP
Area VI	Rot. Optim.	9	37	1	84	81	183	8	354	0.35	1.65	0.22	84	174	12.3	SS	Pure STRIKE-SLIP
2nd Stage: N–S Transension																	
Area II	Rot. Optim.	8	28	5	173	83	306	5	82	0.84	1.16	0.27	173	83	13.6	SS	Extensional STRIKE-SLIP
Area III	Rot. Optim.	14	55	19	199	68	343	12	105	0.66	1.34	0.19	16	106	13	SS	Pure STRIKE-SLIP
Area IV	Rot. Optim.	11	36	1	345	86	231	3	75	0.59	1.41	0.3	165	75	13.9	SS	Pure STRIKE-SLIP
Area VI	Rot. Optim.	7	37	11	169	78	9	4	259	0.19	1.81	0.22	169	79	9	SS	Compressional STRIKE-SLIP
3rd Stage: NE–SW Transpression																	
Area II	Rot. Optim.	10	28	10	56	78	261	5	147	0.31	1.69	0.28	56	146	6.6	SS	Pure STRIKE-SLIP
Area V	Rot. Optim.	24	34	9	225	66	113	22	319	0.18	1.82	0.48	46	136	15.3	SS	Compressional STRIKE-SLIP
Area VI	Rot. Optim.	10	37	1	225	70	318	20	135	0.36	1.64	0.49	45	135	15	SS	Pure STRIKE-SLIP
4th Stage: Extension																	
Area I	Rot. Optim.	16	55	69	356	21	165	4	257	0.33	0.33	0.13	169	79	6.2	NF	Pure EXTENSIVE
Area II	Rot. Optim.	9	28	68	186	0	277	22	8	0.54	0.54	0.19	97	7	212	NF	Pure EXTENSIVE
Area III	Rot. Optim.	15	55	63	311	23	164	13	68	0.65	0.65	0.25	156	66	10.7	NF	Pure EXTENSIVE
All areas																	
1st Stage	Rot. Optim.	68	245	3	270	86	130	2	0	0.09	1.91	0.33	90	0	4.3	SS	Compressional STRIKE-SLIP
2nd Stage	Rot. Optim.	40	245	8	175	81	322	5	84	0.84	1.16	0.23	174	84	9.6	SS	Extensional STRIKE-SLIP
3rd Stage	Rot. Optim.	44	245	7	53	76	294	12	144	0.19	1.81	0.18	53	143	5.9	SS	Compressional STRIKE-SLIP
4th Stage	Rot. Optim.	31	245	77	330	12	172	5	81	0.31	0.31	0.13	169	79	14.3	NF	Pure EXTENSIVE

(green filled dot). During inversion, care was taken to select faults which plot above the line of initial friction in the Mohr diagrams (oblique line with an assumed initial friction angle of  $17^\circ$ ).

In the six different areas, different stages of faulting and related paleostress regimes have been identified (Suppl. 1: Figs. S1–S6). The regional integration of the results allows us to identify four stages that can be correlated throughout the six areas. Note that all stress stages have not been identified in each area.

In order to get a regional representation of the stress regimes, we further processed together all the fault data attributed to each of four stress stages, without performing additional data separation (Fig. 9, Table 1). The regional stress regimes are characterized by the stress regime index  $R'$  and the horizontal stress axes as follows:

1st stage: transpressional regime with a prolate shape of the stress ellipsoid ( $R' = 1.91$ ) and E–W  $SH_{max}$  ( $SH_{max} = N090^\circ E$ );

2nd stage: transtensional regime with oblate shape of the stress ellipsoid ( $R' = 1.16$ ) and N–S  $SH_{max}$  ( $SH_{max} = N174^\circ E$ );

3rd stage: transpressional regime with prolate shape of the stress ellipsoid ( $R' = 1.81$ ) and NE–SW  $SH_{max}$  ( $SH_{max} = N053^\circ E$ );

4th stage: extensional regime ( $R' = 0.31$ ) with E–W  $SH_{min}$  ( $SH_{min} = N074^\circ E$ ).

In the case of a prolate shape of the stress ellipsoid, the strike-slip faulting is associated with a thrust faulting component while in the case of an oblate shape of the stress ellipsoid, the strike-slip faulting is associated with a normal faulting component.

## GEODYNAMIC INTERPRETATION

The 1st stage fault structures are found in most of the investigated areas (I, III, IV, V and VI). The dominant fault system in all study area includes steep NNW–SSE sinistral and WSW–ENE dextral trending faults with subhorizontal striations. Area IV, V, VI are somewhat different in such the NE to ENE trending faults are more common. The fault pattern is best interpreted as conjugate set with subhorizontal principal stress axis trending c. west–east (maximum) and north–south (minimum). The shape factor for the combined data associated with this stress field is around 0.1 although variable values have been derived from individual areas.

Such a stress field releases the above described strike-slip faults as seen in areas I, III and east of area IV (NNW and WSW trending) and tension gashes, in case of prolate stress, that are expected to trend c. west–east at variable dip. This stress field and related strain is compatible with the sinistral wrench tectonic regime as described from the Eastern Desert and correlated with this late Neoproterozoic deformation.

It was concomitant with the assembly of Gondwanaland (D1: Syn-accretion phase in [21]; the first far-field boundary condition in [25]).

The 2nd stage fault pattern includes NE trending sinistral and NW trending dextral faults best seen in areas II, III, IV and VI. The sub-horizontal principal stress axis trend N–S and the shape factor  $R$  is between 0.6 and 0.8 ( $R' = 1.16$  in the average stress tensor), meaning triaxial to oblate stress axes ratios. Such a stress field with similar  $\sigma_1$  and  $\sigma_2$ , and well-defined  $\sigma_3$  would release uniformly N–S trending tension gashes and the described sinistral and dextral shears. Such deformation was characterized by the “extensional collapse” that was kinematically akin to the NNW-ward extrusion of the CED and NED, respectively. The fault-controlled Hammamat basins were formed in pull-apart grabens and fault-related down-sag areas (D2: post-accretion phase in [21]; the second far-field boundary condition in [25]).

The 3rd stage is largely represented in the areas II, V and VI by conjugate system of steep NNE trending dextral and ENE sinistral faults, most of the data derived from area V where a bundle of NE trending dextral shears have been mapped (Fig. 4). It is related to the N to NNE shortening phase that was affecting the Hammamat basins with folding and strike-slip deformation and is defined as the post-Hammamat compression or second phase of shortening in the ENS [15, 19, 20].

The 4th stage is the only stress field with vertical  $\sigma_1$  and W–E to ENE–WSW oriented  $\sigma_3$ . This stress field is derived from ENE–WSW oriented normal faults and few strike-slip faults exposed in areas I, II, III. In the area II, the orientation of  $\sigma_3$  N–S, while in areas I and III, they are ENE–WSW. Since those faults are common in rift-related graben (e.g. area II) correlation with Miocene tectonics is very plausible.

This tectonic phase can depict the retreat of the Cadomian arc [25] particularly in area II and the Red Sea rifting (Oligocene–Miocene) as in areas I and III. The structures formed during this deformation stage are the N- to NNW- striking faults which obviously affected the eastern margin of the Neoproterozoic northern ENS that occupying the western shoulder of the Red Sea-Gulf of Suez rift.

## DISCUSSION

The processing of Landsat 8 images using different remote sensing techniques (FCC, OIF, PCA, MNF and BR) indicates the predominance of post-orogenic granitoids, Dokhan Volcanics and Hammamat molasse sediments, dissected by dyke swarms and extensional fractures, veins and pegmatites. This lithology led many authors to consider the northern ENS as an extensional domain, based on the mode of occurrence and the formation conditions of the previously mentioned rock units [11].



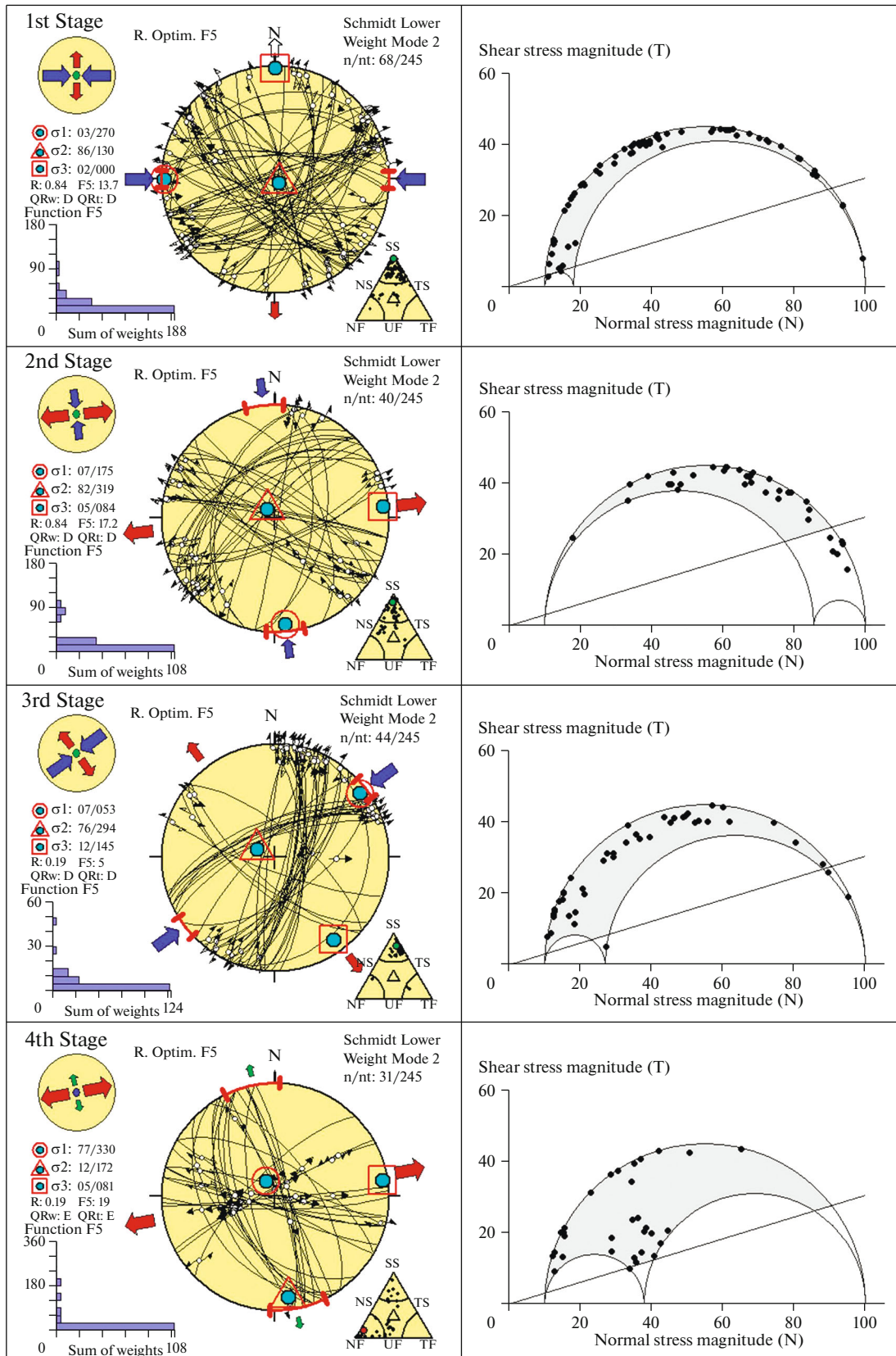


Fig. 9. Stress stages 1st–4th obtained from the processing of all fault data collected from areas I–VI.

However, we suggest an alternative model for the northern province of the ENS. According to our results, the area north of Safaga–Qena deformation/shear belt until the tip of the Neoproterozoic ENS is characterized by a protracted brittle-ductile deformation history. Although the old structures and rock collages are entirely masked by voluminous masses of different types of granitoids, Dokhan Volcanics and Hammamat Sediments, the fault striae analysis and paleostress reconstruction performed here demonstrate that four successive brittle deformational stages affected the entire province.

The general idea that the NED is a pure extensional domain must therefore be modified. We propose instead that the NED is a complex tectonic province that has been deformed by two strike-slip faulting stress stages with prolate shape of the stress ellipsoid separated by a slip faulting stress stage with oblate shape of the stress ellipsoid (transtensional phase). It was later affected by normal faulting during both late Neoproterozoic–Cambrian time (retreat of the Cadomian arc [40]) and the Oligocene–Miocene rifting along the Gulf of Suez and Red Sea.

## CONCLUSIONS

(1) The northern tectonic province of the ENS has experienced four successive phases of deformation which are successfully restored using fault striae analysis and paleostress reconstruction methods. The field geology supplemented by LANDSAT-based lithological mapping techniques support the general agreement that the northern ENS developed through a regional phase of extensional tectonic deformation. The obtained results indicate a sequence of transpressional and transtensional deformational stages, followed by a normal faulting one.

(2) The strike-slip faulting regime stages reflect successively regional  $SH_{max}$  patterns oriented N090° E, N174° E and N053° E. The normal-faulting regime correspond to a regional  $Sh_{min}$  oriented N074° E. Such deformational regimes have been concurrently associated with four tectonic events; E–W shortening due to oblique convergence between E and W Gondwana, northward migration of the CED and NED causing orogen-parallel extensional collapse, N–S shortening post-dating the Hammamat sedimentation and normal faulting related to the retreat of the Cadomian Arc and afterwards the Red Sea–Gulf of Suez rifting.

## ACKNOWLEDGMENTS

We would like to thank the editorial board members of the *Geotectonics Journal* and anonymous reviewers for their thorough and constructive comments that significantly improved the earlier version of the manuscript. Special thanks are extended to editor Marina N. Shoupletsova (GIN RAS, Moscow, Russia).

We are also indebted and grateful to the driver Mohamed Saad for his great help during field trips.

## COMPLIANCE WITH ETHICAL STANDARDS

Authors declare that they have no conflict of interests.

## OPEN ACCESS

This article is licensed under a Creative Commons Attribution 4.0 International License, which permits use, sharing, adaptation, distribution and reproduction in any medium or format, as long as you give appropriate credit to the original author(s) and the source, provide a link to the Creative Commons license, and indicate if changes were made. The images or other third party material in this article are included in the article's Creative Commons license, unless indicated otherwise in a credit line to the material. If material is not included in the article's Creative Commons license and your intended use is not permitted by statutory regulation or exceeds the permitted use, you will need to obtain permission directly from the copyright holder. To view a copy of this license, visit <http://creativecommons.org/licenses/by/4.0/>.

## SUPPLEMENTARY INFORMATION

The online version contains supplementary material available at <https://doi.org/10.1134/S001685212304009X>.

## REFERENCES

1. A. M. Abdel-Rahman and R. F. Martin, "Late Pan-African magmatism and crustal development in north-eastern Egypt," *Geol. J.* **22**, 281–301 (1987).
2. M. J. Abrams, D. Brown, L. Lepley, and R. Sadowski, "Remote sensing for porphyry copper deposits in Southern Arizona," *Econ. Geol.* **78**, 591–604 (1983).
3. E. M. Anderson, *The Dynamics of Faulting and Dyke Formation with Applications to Britain* (Oliver & Boyd, Edinburgh, UK, 1951).
4. J. Angelier, Fault slip analysis and palaeostress reconstruction, in *Continental Deformation*, Ed. by P. L. Hancock (Pergamon Press, Oxford, UK, 1994), pp. 53–100.
5. M. Bott, "The mechanics of oblique slip faulting," *Geol. Mag.* **96**, 109–117 (1959).
6. D. Delvaux, "Win-Tensor, an interactive computer program for fracture analysis and crustal stress reconstruction," EGU General Assembly (Vienna, Austria), *Geophys. Res. Abstr.* **13**, 2011–4018 (2011).
7. D. Delvaux, "Release of program Win-Tensor 4.0 for tectonic stress inversion: Statistical expression of stress parameters," EGU General Assembly (Vienna, Austria), *Geophys. Res. Abstr.* **14**, 2012–5899 (2012). <https://doi.org/10.13140/RG.2.2.23415.62887>
8. D. Delvaux, R. Moeys, G. Stapel, C. Petit, K. Levi, A. Miroshnichenko, V. Ruzhich, and V. Sankov, "Paleostress reconstructions and geodynamics of the Baikal region, Central Asia. Part II: Cenozoic rifting," in *Structural Controls on Sedimentary Basin Formation*, Ed. by S. Cloetingh, M. Fernandez, J. A. Munoz, W. Sas-

- si, and F. Horvath (Tectonophysics, Vol. 282, pp. 1–38, 1997).
9. D. Delvaux and B. Sperner, “New aspects of tectonic stress inversion with reference to the TENSOR program,” in *New Insights into Structural Interpretation and Modelling*, Ed. by D. Nieuwland (Spec. Publ.—Geol. Soc. London, 2003, Vol. 212), pp. 75–100.
  10. W. M. Dunne and P. L. Hancock, “*Palaeostress Analysis of Small-Scale Brittle Structures*,” in *Continental Deformation*, Ed. by P. L. Hancock (Pergamon Press, Oxford, UK, 1994), pp. 101–120.
  11. M. Z. El-Bialy and M. M. Omar, “Spatial association of Neoproterozoic continental arc I-type and post-collision A-type granitoids in the Arabian–Nubian Shield: the Wadi Al-Baroud older and younger granites, North Eastern Desert, Egypt,” *J. Afr. Earth Sci.* **103**, 1–29 (2015).
  12. H. A. Eliwa, C. Breitzkreuz, M. Murata, I. M. Khalaf, B. Bühler, T. Itaya, T. Takahashi, Y. Hirahara, T. Miyazaki, J.-I. Kimura, T. Shibata, Y. Koshi, Y. Kato, H. Ozawa, M. A. Daas, and Kh. El Gameel, “SIMS zircon U–Pb and mica K–Ar geochronology, and Sr–Nd isotope geochemistry of Neoproterozoic granitoids and their bearing on the evolution of the north Eastern Desert, Egypt,” *Gondwana Res.* **25** (4), 1570–1598 (2014).
  13. M. M. El-Sayed, M. H. Shalaby, and M. A. Hassanen, “Petrological and geochemical constraints on the tectonomagmatic evolution of the Late Neoproterozoic granitoid sites in the Gattar area, North Eastern Desert, Egypt,” *Neues Jahrb. Mineral., Abh.* **178**, 239–275 (2003).
  14. H. Fossen, *Structural Geology* (Cambridge Univ. Press, Cambridge, UK, 2010).
  15. A. Fowler and Z. Hamimi, “Structural and tectonic framework of Neoproterozoic basement of Egypt: from gneiss domes to transpression belts,” in *The Geology of Egypt*, Ed. by Z. Hamimi, A. El-Barkooky, J. Martínez Frías, H. Fritz, and Y. Abd El-Rahman (Springer Nature, Switzerland, Reg. Geol. Rev., 2020), pp. 81–129. [https://doi.org/10.1007/978-3-030-15265-9\\_3](https://doi.org/10.1007/978-3-030-15265-9_3)
  16. M. H. Francis, “Geology of the basement complex in the North Eastern Desert between latitudes 25°30′ and 26°30′ N,” *Ann. Geol. Surv. Egypt* **II**, 161–180 (1972).
  17. C. Frohlich, “Triangle diagrams: ternary graphs to display similarity and diversity of earthquake focal mechanisms,” *Phys. Earth Planet. Interiors* **75**, 193–198 (1992).
  18. I. G. Gass, “Upper Proterozoic (Pan-African) calc-alkaline magmatism in north-eastern Africa and Arabia,” in *Andesites*, Ed. by R. S. Thorpe (Wiley, NY, USA, 1982), pp. 591–609.
  19. R. O. Greiling, M. M. Abdeen, A. A. Dardir, H. El Akhal, M. F. El Ramly, G. M. Kamal El Din, A. F. Osman, A. A. Rashwan, A. H. Rice, and M. F. Sadek, “A structural synthesis of the Proterozoic Arabian–Nubian Shield in Egypt,” *Geol. Rundsch.* **83**, 484–501 (1994).
  20. W. Hagag, Z. Hamimi, and A. Abdelnasser, “The effect of the Najd shear deformation on the Pan-African belt of the central Egyptian Nubian Shield: A synthesis for the post-collision tectonic events,” *J. Asian Earth Sci.* **224**, 105022 (2022). <https://doi.org/10.1016/j.jseaeas.2021.105022>
  21. Z. Hamimi, M. b. A. Abd El-Wahed, H. A. Gahlan, and S. Z. Kamh, “Tectonics of the Eastern Desert of Egypt: A key to understanding the Neoproterozoic evolution of the Arabian–Nubian Shield (East African Orogen),” in *Geology of the Arab World—An Overview*, Ed. by A. Bendaoud, Z. Hamimi, M. Hamoudi, S. Djemai, and B. Zoheir (Springer Geol., NY, USA, 2019), pp. 1–81. [https://doi.org/10.1007/978-3-319-96794-3\\_1](https://doi.org/10.1007/978-3-319-96794-3_1)
  22. Z. Hamimi, S. Arai, A. Fowler, and M. Z. El-Bialy, *The Geology of the Egyptian Nubian Shield* (Springer Nature, Switzerland, RGR, 2021). <https://doi.org/10.1007/978-3-030-49771-2>
  23. Z. Hamimi, A. El-Barkooky, J. Martínez Frías, H. Fritz, and Y. Abd El-Rahman, *The Geology of Egypt* (Springer Nature Switzerland, RGR, 2020). [https://doi.org/10.1007/978-3-030-15265-9\\_2](https://doi.org/10.1007/978-3-030-15265-9_2)
  24. Z. Hamimi, M. El-Shafei, G. Kattu, and M. Matsah, “Transpressional regime in southern Arabian Shield: Insights from Wadi Yiba Area, Saudi Arabia,” *Min. Petrol.* **107**, 849–860 (2013).
  25. Z. Hamimi, W. Hagag, H. Fritz, H. Baggazi, and S. Kamh, “The tectonic map and structural provinces of the Late Neoproterozoic Egyptian Nubian Shield: Implications for crustal growth of the Arabian–Nubian Shield (East African Orogen),” *Front. Earth Sci.* **10**, 921521 (2022). <https://doi.org/10.3389/feart.2022.921521>
  26. Z. Hamimi, A.-R. Fowler, J.-P. Liegeois, A. Collins, M. Abdelsalam, and M. Abd El-Wahed, *The Geology of the Arabian–Nubian Shield* (Springer Nature, Switzerland, RGR, 2021). <https://doi.org/10.1007/978-3-030-72995-0>
  27. M. A. Hassan and A. H. Hashad, “Precambrian of Egypt” in *The Geology of Egypt*, Ed. by R. Said (Balke-ma, Rotterdam, The Netherlands, 1990), pp. 201–245.
  28. A. A. Hussein, M. M. Aly, and M. F. El Ramly, “A proposed new classification of the granites of Egypt,” *J. Volcanol. Geotherm. Res.* **14**, 187–198 (1982).
  29. P. R. Johnson, A. Andresen, A. S. Collins, A. R. Fowler, H. Fritz, W. Ghebreab, T. Kusky, and R. J. Stern, “Late Cryogenian–Ediacaran history of the Arabian–Nubian Shield: A review of depositional, plutonic, structural, and tectonic events in the closing stages of the northern East African orogeny,” *J. Afr. Earth Sci.* **61**, 167–232 (2011).
  30. M. L. Kipata, D. Delvaux, M. N. Sebagenzi, J. -J. Cail-teux, and M. Sintubin, “Brittle tectonic and stress field evolution in the Pan-African Lufilian arc and its foreland (Katanga, DRC): From orogenic compression to extensional collapse, transpressional inversion and transition to rifting,” *Geol. Belgica* **16** (1–2), 1–17 (2013).
  31. O. Lacombe, “Do fault slip data inversions actually yield “paleostresses” that can be compared with contemporary stresses? A critical discussion,” *C. R. Geosci.* **344**, 159–173 (2012).
  32. B. Lund and J. Townend, “Calculating horizontal stress orientations with full or partial knowledge of the tectonic stress tensor,” *Geophys. J. Int.* **170**, 1328–1335 (2007).
  33. A. M. Moghazi, “Magma source and evolution of Late Neoproterozoic granitoids in the Gabal El-Urf area,



- Eastern Desert, Egypt: Geochemical and Sr–Nd isotopic constraints,” *Geol. Mag.* **163**, 285–300 (1999).
34. A. M. Moghazi, “Petrology and geochemistry of Pan-African granitoids, Kab Amiri area, Egypt—Implications for tectonomagmatic stages of the Nubian Shield evolution,” *Min. Petrol.* **75**, 41–67 (2002).
  35. C. Pascal, *Paleostress Inversion Techniques—Methods and Applications for Tectonics* (Elsevier, NY, USA, 2022).
  36. U. Riller, M. D. Clerk, H. Daxberger, D. Doman, L. Lenauer, S. Plath, and T. Santiamo, “Fault-slip inversions: Their importance in terms of strain, heterogeneity, and kinematics of brittle deformation,” *J. Struct. Geol.* **101**, 80–95 (2017).
  37. F. F. Sabins, *Remote Sensing Principles and Interpretation*, 3rd ed. (W. H. Freeman, NY, USA, 1997, Vol. 10).
  38. J. L. Simon, “Forty years of paleostress analysis: has it attained maturity?” *J. Struct. Geol.* **125**, 124–133 (2019).
  39. B. Sperner, L. Ratschbacher, and R. Ott, “Fault-striae analysis: A turbo pascal program package for graphical presentation and reduced stress tensor calculation,” *Comp. Geosci.* **19**, 1361–1388 (1993).  
[https://doi.org/10.1016/0098-3004\(93\)90035-4](https://doi.org/10.1016/0098-3004(93)90035-4)
  40. R. J. Stern, K. A. Ali, M. Ren, Gh. H. Jarrar, R. Romer, M. I. Leybourne, M. J. Whitehouse, and Kh. M. Ibrahim, “Cadomian (~560 Ma) crust buried beneath the northern Arabian Peninsula: Mineral, chemical, geochronological, and isotopic constraints from NE Jordan xenoliths,” *Earth Planet. Sci. Lett.* **436**, 31–42 (2016).
  41. R. J. Stern and C. E. Hedge, “Geochronologic and isotopic constraints on Late Precambrian crustal evolution in the Eastern Desert of Egypt,” *Am. J. Sci.* **258**, 97–127 (1985).
  42. S. A. Wilde and K. Youssef, “A re-evaluation of the origin and setting of the Late Precambrian Hammamat group based on SHRIMP U–Pb dating of detrital zircons from Gabal Umm Tawat, North Eastern Desert, Egypt,” *J. Geol. Soc. London* **159**, 595–604 (2002).
  43. M. L. Zoback, M. D. Zoback, J. Adams, M. Assumpcao, S. Bell, E. A. Bergman, P. Blümling, N. R. Brereton, D. Denham, J. Ding, K. Fuchs, N. Gay, S. Gressersen, H. K. Gupta, A. Gvishiani, K. Jacob, R. Klein, P. Knoll, M. Magee, J. I. Mercier, B. C. Müller, C. Paquin, K. Razjendran, O. Stephansson, G. Suarez, M. Suter, A. Udias, Z. H. Xu, and M. Zhizhin, “Global patterns of tectonic stress,” *Nature* **341** (6240), 291–298 (1989).
  44. Environment for Visualizing Images v5.1, (ENVI; Harris Geospatial Solutions, Broomfield, CO, USA), <https://www.13harrisgeospatial.com> (Accessed March, 2023).
  45. Landsat 8, <http://earthexplorer.usgs.gov> (Accessed March, 2023).